WAVE PROPAGATION IN HIGHLY HETEROGENEOUS MEDIA: SCALABILITY OF THE MESH AND RANDOM PROPERTIES GENERATOR

J. J. Camata[1], L. A. Corrêa[2], L. C. Paludo[2], L. Aubry[3], R. Cottereau[2], A. L. G. A. Coutinho[1]

[1] *COPPE/Federal University of Rio de Janeiro, Brazil*
[2] *MSSMat, CNRS, CentraleSupelec, Universite Paris-Saclay, France*
[3] *CEA, DAM, DIF, 91297 Arpajon Cedex, France*

Abstract

Direct numerical simulation of wave propagation in highly heterogeneous media demands very fine discretization in space and time, and scalability of all steps of a numerical simulation, including the pre- and post-processing. In this paper, we integrate the following elements in a scalable parallel workflow: an octree meshing scheme, a random field generator for mechanical properties, and a spectral element solver for wave propagation. The hexahedral meshing algorithm includes the consideration of topography, bathymetry, coastlines and wave velocity variation with depth. The random field generator allows to modify locally (in space) the value of a given realization. Numerical simulations and scalability studies are presented for each and all components of the seismic simulation workflow.

Keywords: Meshing, Random media, Elastic wave propagation, Parallel computing, Scalability analysis

1. Introduction

Exploration of the structure of the Earth using seismograms recorded at the surface is a classical problem in geophysics. Its applications range from the scientific understanding of Earth's interior to more industrially-oriented questions related to oil exploration or CO2 and nuclear waste sequestration. Current methods of elastic tomography in geophysical media are mainly based on the arrival times of the first waves. With this information, geophysicists manage to represent reasonably well very low-frequency waves using, e.g., spherically-symmetric Earth models with homogeneous layers. At a more regional scale, seismic tomography methods such as Reverse Time Migration yield reasonably accurate models of underground mechanical structures, such as those found in oil reservoirs. However, geological observations as well as recordings in the higher frequency range indicate a strong heterogeneity of the crust [1]–[7]. Recent inversion techniques try to go beyond classical identification methods by considering full waveform inversion [8] rather than relying on first arrivals only, and to identify finer-scale structures.

The most obvious impact of these heterogeneities is the creation of the coda [9]–[11], which is a seemingly random wave train behind the first coherent arrivals, and may last much longer than the first pulses. More generally, the heterogeneities have a large influence on the wave fields at the surface [12], and their consideration in an inversion scheme requires a profound understanding of that influence. Based on asymptotic analyses, theoretical models have been introduced, such as radiative transfer and diffusion models [13]–[15]. Although these models are difficult to use in actual inversion schemes because they are derived in theoretical settings (unbounded domains and material isotropy for instance), they help acknowledge the fact that the influence of the small scale heterogeneities is statistical in nature. This means that different materials with similar statistical distribution of the parameters would yield statistically similar features of the wave field. In an inversion scheme, one should therefore be more interested in identifying the statistical parameters of these small-scale heterogeneities rather than point-wise values. For classical inversion methods based on direct numerical simulations and minimization of a cost function, one is therefore led to consider large scale wave propagation simulations in realizations of random media.

Research effort has been devoted to the development of high performance schemes for large scale wave propagation. Solvers can now scale efficiently over very large clusters [16]–[18]. The pre- and post-processing steps have not necessarily followed the same pace. Although various techniques and algorithms have been developed [19], octree-based meshing has recently demonstrated improved capabilities for scaling over today's largest machines [20]–[25]. The need to generate randomly heterogeneous fields of mechanical parameters for geophysics has emerged later [6], [26]–[32] and scaling of the current algorithms has only been recently tackled [33], [34]. The scalability of the entire wave propagation workflow is limited by its slowest link. The main objective of this paper is therefore to demonstrate the scalability of each and all of the ingredients of the simulation and to integrate them seamlessly. Along the path, improvements on the meshing algorithm and random field generation will be presented, specifically tailored for geophysics applications. This includes the consideration of topography, bathymetry, coastlines and wave velocity evolution with depth for the meshing algorithm, and introducing the possibility of modifying locally (in space) the value of a realization of the random field.

The remainder of this paper is organized as follows. In the next section, we briefly review the elastic wave equations and the spectral element approximation that is chosen for this work. Section 3 describes our parallel octree-based mesh generator. We introduce in Section 4 our parallel random field generator. A numerical simulation example is presented in Section 5 and the paper ends with a summary of our main conclusions and future research directions.

2. Spectral element solver for elastic wave propagation

Elastic wave propagation describes the evolution in a domain Ω and over a time interval $(0, T)$ of a displacement field $u(x, t)$ driven by the following equation (1):

$$\rho(x)\acute{u}(x, t) - \nabla \cdot \sigma(x, t) = f(x, t) \tag{1}$$

when submitted to loading $f(x, t)$ and initial conditions $u(x, t = 0) = u_0(x)$ and $\acute{u}(x, t = 0) = v_0(x)$. In this equation, the superimposed dot stands for derivation with respect to time and the stress tensor $\sigma(x, t) = C(x): \epsilon(x, t)$ is related to the strain tensor $\epsilon = (\nabla u + \nabla u^T)/2$ through the constitutive tensor $C(x)$. In geophysics, Ω is usually partly unbounded, and a homogeneous Neumann boundary condition $\sigma \cdot n = 0$ is considered at the free surface Γ.

In this paper, we use the spectral element method (SEM) [35], [36]. A conformal hexahedral mesh is constructed (see Section 3), and the approximation in space of Eq. 1 is performed using Lagrange polynomials of high order (typically order 5 to 7) over elements of that mesh. The nodes of the Lagrange polynomials are those of the Gauss-Lobatto-Legendre (GLL) quadrature so that $N_i(x_i) = 1$, and $N_i(x_{i \neq j}) = 0$ for all polynomials N_i and quadrature points x_i. The stiffness matrix K is defined by $K_{ij} = \int_\Omega \nabla N_i : C : \nabla N_j d\Omega$. The mass matrix M is defined by $M_{ij} = \int_\Omega \rho N_i \cdot N_j d\Omega$. The integrals are evaluated with the GLL quadrature corresponding to the nodes of the polynomials so the mass matrix is naturally diagonal.

For time discretization, we consider a second-order explicit scheme. This scheme is conditionally stable under the Courant-Friedrich-Levy (CFL) condition $\Delta t \leq \alpha h / v_p$, where h is the smallest distance between two GLL nodes, v_p is the largest wave velocity (P-wave velocity for isotropic materials), and α is a safeguard constant, usually taken as $\alpha = 0.25$ for SEM simulations [37], [38]. To cope with the truncated domain, we are using Perfectly Matched Layers (PMLs) [39], in a stress-velocity formulation [40]. These developments were implemented in a parallel code developed jointly by Commissariat à l''Energie Atomique, Institut de Physique du Globe and CentraleSupélec. This code was used to simulate the passage of a seismic wave in a sedimentary basin over 2048 cores [42]. Table 1 shows good scalability of the solver up to 4096~cores for a 3D simulation of wave propagation in a homogeneous space with 7 GLL nodes in each direction and element and with no PMLs. These scaling tests were performed on Tera100 (at Bruyères-le-Châtel, France) a BULL machine equipped with almost 140,000 Intel Xeon 7500 processor cores.

Table 1 - Wave propagation simulation times per time step

Cores	DOFs	Elements	Avg. Time [s]	Min Time [s]
32	36,026,967	55,296	0.204	0.198
128	141,137,643	221,184	0.212	0.200
512	558,508,233	884,736	0.256	0.208
4096	4,527,010,569	7,077,888	0.362	0.256

3. Scalable parallel mesher for geophysical applications

Meshing is particularly hard considering high-resolution wave propagation problems using conformal hexahedra in realistic Earth geometries [19]. Here, high resolution means meshes containing several billions of elements. For such large meshes octree-based algorithms seem to be particularly susscessful [22], [23]. Octrees are spatial data structures used in various problems in computer science and engineering, e.g., object representation, image analysis and unstructured meshing [41]. Standard octrees divide a cell into eight new cells. However, it has been shown that a 3-octree, defined as a data structure where a cell is divided into 27 new cells [42] is more suitable for hexahedral mesh generation.

3.1 Mesh with depth-dependent element size

For wave propagation problems, the main parameter controlling the size of the elements is the wave velocity. In geophysical problems, there is on average a gradient of this velocity with depth, with lower velocities closest to the surface of the Earth. In this first step of our procedure, we therefore aim at constructing a mesh where the elements are homogeneous along the horizontal planes and are larger in depth than close to the surface. The construction must also avoid hanging nodes, since the SEM code discussed in Section 3 requires a conformal mesh. The procedure to create the hexahedra starts with the finest cells (closest to the surface). Every m meters (input parameter, chosen by the user and related to the wave velocity map), a transition layer is introduced. This layer is composed of cells shown in Fig 1 (and based on [19]), that allow to reduce the size of the elements between two layers. The whole process is done in parallel. The domain is initially partitioned in a 2D grid among processes, and the construction is done independently by each process. The output of this step of the construction is a structured mesh.
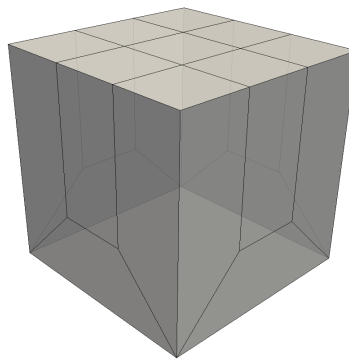

Fig 1 - 13-cell template used in the transition layers between coarse and fine elements.

3.2 Consideration of topography and ocean level

In order to represent realistic Earth geometries, a smooth scheme [43] is used to fit the octree mesh with a surface triangulation (STL) generated from SRTM3 topography data [44] sampled at three arc-seconds, and obtained from United States Geological Survey [45]. This STL file includes the topography (inland heights) and the altitude is set to zero over oceans and seas. The output of this step of the construction is still a structured mesh, but with deformed elements.

3.3 Consideration of bathymetry and material interfaces

Realistic meshes of the Earth must also include the representation of the bathymetry, as well as various materials interfaces [46] inside the Earth (e.g. basins inducing strong site effects, Moho discontinuity, or others). With respect to the mesh constructed at the previous step, the bathymetry can be seen as material discontinuity (between solid and fluid) so we only describe in this paper the inclusion of bathymetry. The bathymetry is defined through a STL surface, constructed from the SRTM30_PLUS model [47], a 30-arc second resolution global topography/bathymetry grid obtained from Scripps Institution of Oceanography, University of California San Diego [48]. This STL surface is defined on a regular grid and is modified in the following manner: nodes at vanishing altitude are added along the coastline, using the information stored in the SRTM water body database [49], and inland nodes are removed. A 2D Delaunay triangulation is then used to construct a new STL containing only the fluid-solid interface. Other types of material or interface discontinuity can be treated similarly, through the definition of an appropriate STL file.

Some of the hexahedra constructed at the previous step are intercepted by this STL surface. For the final mesh to conform to the material interface, these hexahedra should be further divided. We have implemented three subdivision templates that cover all the possibilities for an intersection between a hexahedron and the STL surface. These templates are shown in Fig 2. Template 1 is applied when the STL surface cuts four non-contiguous edges and cuts the original element in two new elements. Template 2 is applied when the STL surface intercepts all the faces connected to the same edge and cuts the original element in three new elements.

Template 3 is applied when the STL surface intercepts all the faces connected to the same vertex and cuts the original element in four new elements. If some of the new elements are degenerated and show angles equal or above 180° a pillowing technique can be used [50]. After this entire process, the MESQUITE library [51] may be used to relocate vertices and improve the mesh quality.
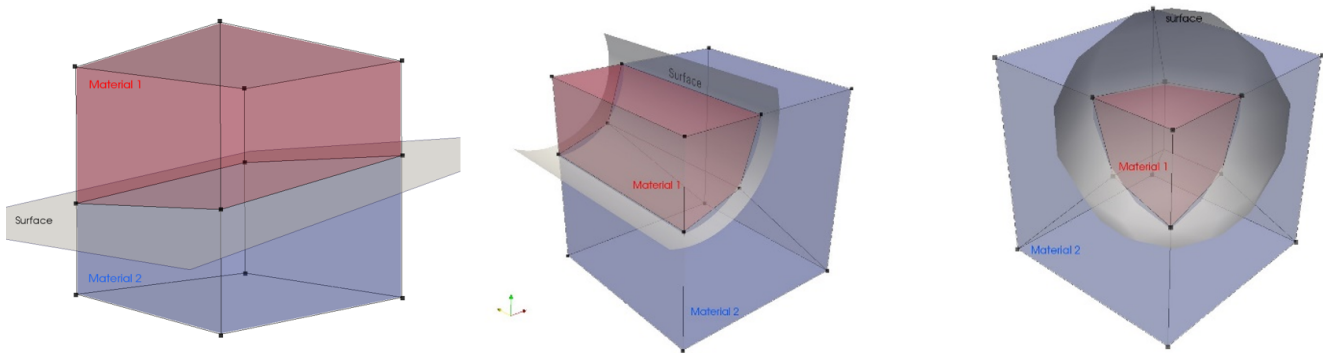

Fig 2 - Subdivision templates used for separating subdividing hexahedra crossed by the material interface. The colors indicate different materials and the grey surface indicates the material interface.

3.4   Example of mesh generation

The final mesh is a non-structured hexahedral mesh, conformal to the topography, bathymetry and coastlines and with coarsening of the elements with depth. An example of mesh generated with the proposed scheme is presented in Fig 3. This mesh was generated on Occigen (at CINES, France), a BULL machine equipped with 2106 computing nodes. Each Occigen node has two Intel Haswell (E5-2690) processor (12 cores per node), totalizing 50544 cores. The example considers Kefalonia region in Greece (between N 38°00'00 E 20°00' and N 39°00' E 21°00') in a cube of approximately 110 X 110 X 110 km^3. The bathymetry goes down to 3790 m and the topography up to 1620 m. The mesh grading with depth, as well as the features of the topography and bathymetry can be seen in – Meshing example of Kefalonia region in GreeceFig 3.
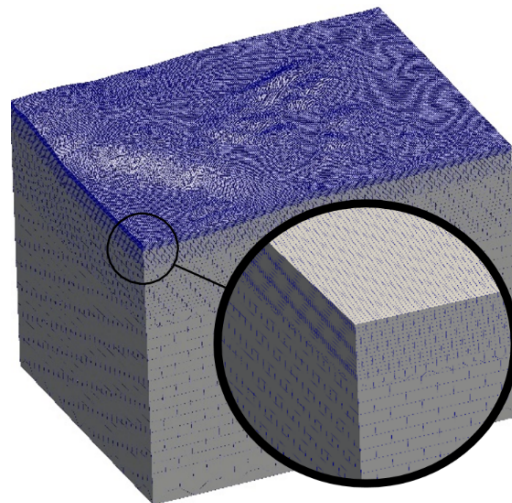

Fig 3 – Meshing example of Kefalonia region in Greece, the zoom shows how mesh changes with depth.

3.5   Weak scalability analysis

We perform a weak scalability analysis of the parallel mesh generator on Occigen for the same case discussed in Section 3.4 (Kefalonia region in Greece). We analyse how the CPU time varies with the number of cores for a

constant amount of data per core. In our analysis, this amount of data is defined by the number of elements resulting from the meshing algorithm. Table 2 shows the growth in problem size according to the number of cores. Note that, for each increase in the octree refinement level, the mesh size grows by a factor of 9, reaching 62 billions of hexahedra at level 10. Table 2 also presents the overall CPU time (in seconds) for runs instrumented by TAU performance analysis system [52], [53] on Occigen, using its standard configuration on this system. Although the run time increases almost 3 times when refinement levels increase from 7 to 9, note that, for each level, the mesh size grows by a factor of 9, while the number of cores increases only by a factor of 3. From 9 to 10 refinement levels, we observe that both the mesh size and cores grow by the same factor. In this case, the additional refinement level increases run time in about 20%. Table 2 also reveals that increasing the number of octree levels does not increase the computation/communication ratio, which stays below 30%.

Table 2 - Weak scaling of the mesh generation for the Kefalonia region in Greece.

Cores	Levels	Nodes	Elements	Time [s]	Comm(%)
81	7	85,602,744	83,102,679	12.061	21 %
243	8	769,790,232	747,937,476	32.994	20 %
729	9	6,926,153,724	6,731,438,013	105.188	25 %
6561	10	62,330,385,168	60,583,119,264	123.066	29 %

4. Scalable parallel random field generation

4.1 Classical schemes for random field generation

For direct numerical simulation in highly heterogeneous media, realizations of stationary random fields of mechanical properties (for example Lamé coefficient $\mu(x)$) with given statistics have to be generated at N_p points in Ω. These points are the GLL integration points used in the wave propagation solver to assemble the mass and stiffness matrices. The statistics are usually the average and the autocovariance $R(x)$ of the mechanical properties. There are essentially two classes of techniques, either generating in the space domain or in the spectral domain, but all relying on the generation of a Gaussian random field $g(x)$ and its subsequent transformation through a point-wise non-linear map (e.g., the Rosenblatt transform [54]) into the desired first-order marginal density, for example log-normal, for the mechanical property at hand. In the former case [61], a covariance matrix R is assembled, such that $R_{ij} = R(x_i - x_j)$, where the $\{x_i\}_{1 \le i \le N_p}$ are the N_p points where the random field is to be generated. The most computationally intensive part of the generation algorithm in space is the Cholesky factorization of R, which scales as $O(p^N|\ |3)$ in the general case, but can be improved to sub-

$O(p^N|\ |2)$ using a polynomial approximation of the Cholesky factor [33]. On the other hand, working in the wave number domain, the spectral representation technique [55] expands the random field $g(x)$ as Equation 2:

$$g(x) = \sum_{n \leq N} \sqrt{2S(k_n) \lor \Delta k \lor \cos\left(\quad \right)} \quad k_n \cdot x + \mathring{\phi}_n \tag{2}$$

where the spectral domain k is discretized over a regular grid of size $N = \left[N_x, N_y, N_z\right]$ and indexed by $n = \left[n_x, n_y, n_z\right]$, $S(k_n)$ is the power spectral density of the random field (Fourier transform of $R(x)$), $\Delta k \lor$ is the unit volume in the spectral domain and the random variables $\mathring{\phi}_n$ are the independent elements of a N-dimensional random variable with uniform density over $[0, 2\pi]$. The complexity of that generation scheme in the space domain is $O(p| \quad |2)$ and can be improved to $O\big(N log(N)\big)$ using the Fast Fourier Transform [55]. In that latter case, since the GLL points are not uniformly distributed in space, the random field must be generated on a uniform grid before it is interpolated at the desired N_p GLL nodes.

4.2   Localization of the random field generation

When propagating waves over distances much larger than the correlation length of the mechanical properties, the number of GLL points N_p increases, even for low frequencies. Indeed, both the wavelength and the correlation length must be resolved by the mesh. As the generation schemes are all super-linear, they become a bottleneck for the kind of simulations considered in Table 2. The scalability issue arises because the random field is assumed correlated over the entire domain Ω. In most interesting cases, however, the correlation length is much smaller than the characteristic domain size. It is then possible [34] to generate realizations of $g(x)$ over the entire domain as superpositions of I smaller independent realizations $g_i(x)$ supported on overlapping subdomains Ω_i of Ω:

$$g(x) = \sum_{i \in I} \sqrt{\psi_i(x)} g_i(x) \tag{3}$$

where the set of functions $\psi_i(x)$ forms a partition of unity of Ω (that is to say $\sum_{i \in I} \psi_i(x) = 1$ for any $x \in \Omega$), supported by the set of subdomains Ω_i. Using this approach, the complexity becomes $O\left(n_p log\left(n_p\right)\right)$ where $n_p = N_p / P$ and P is the number of processors. Essentially, this means that the scheme is $O(1)$ when we consider a constant number of GLL nodes per processor. The overlapping Eq. 3 involves an approximation that does not alter the average and variance of the resulting field $g(x)$ [35]. The influence on the correlation structure depends on the overlap, relative to the correlation length. Theory and numerical tests have shown [35] that a transition volume of 5 to 10 correlation length is enough to make statistics homogeneous over the whole domain.

An illustration of Equation 3 is presented in Fig 4 for two processors in 1D. The first processor generates a field $g_1(x)$ over [0-125] km, the second processor generates a field $g_2(x)$ over [25-150] km, and the overlapping area is [25-125] km. The partition of unity is composed of linear functions $\psi_1(x)$ and $\psi_2(x) = 1 - \psi_1(x)$ in the overlap. The upper plots of Fig 4 present in thin continuous lines the two fields $g_1(x)$ (top left) and $g_2(x)$ (top right), as well as the functions $\sqrt{\psi_1(x)}$ (top left) and $\sqrt{\psi_2(x)}$ (top right) in dashed lines. The lower plot of Fig 4 presents the field $g(x)$ reconstructed over [0-150] km using Equation 3. Finally, an example of a 3D realization is presented in Fig 4.
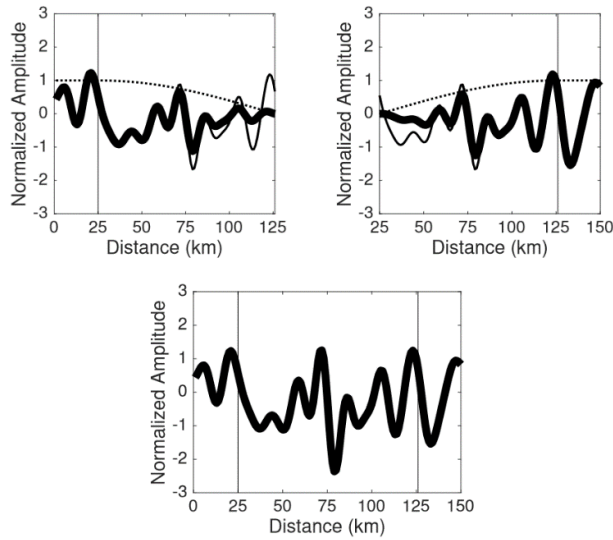
Fig 4 - Generation of two independent samples (thin solid lines) $g_1(x)$ (top left) and $g_2(x)$ (top right), with their respective weight functions $\sqrt{\psi_1(x)}$ (top left) and $\sqrt{\psi_2(x)}$ (top right) (dashed lines). The thick solid lines represent the products $\sqrt{\psi_1(x)}g_1(x)$ (top left) and $\sqrt{\psi_2(x)}g_2(x)$ (top right) and the reconstructed global random field $g(x)$ (lower plot) given by Eq 3.
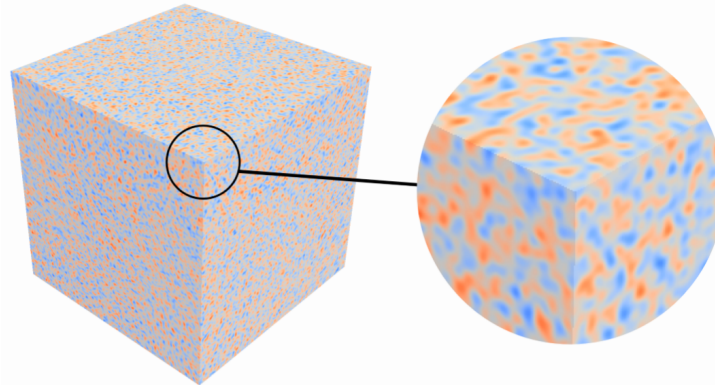

Fig 5- Example of 3D random field generated over 27 procs using the localized approach. The cube edge length is 70 km and the correlation lenth is 1 km. The sampling took 9 minutes (Wall time).

Note that the generation of the local fields $g_i(x)$ in this paper are performed with the spectral representation methods. However, Equation 2 could be replaced without any difficulty by any other method, such as those based on the Cholesky factorization.

4.3   Weak Scalability Analysis

We perform a weak scalability analysis of the random field generator on Igloo cluster (Intel Xeon X7542 2.66Ghz/800 cores) to compare the standard generation with the one using the localized approach. The difference is clear. The expected $O(1)$ scalability is proven by the the plateau showed in Fig 6 and as a result the properties generation suits large scale problems.
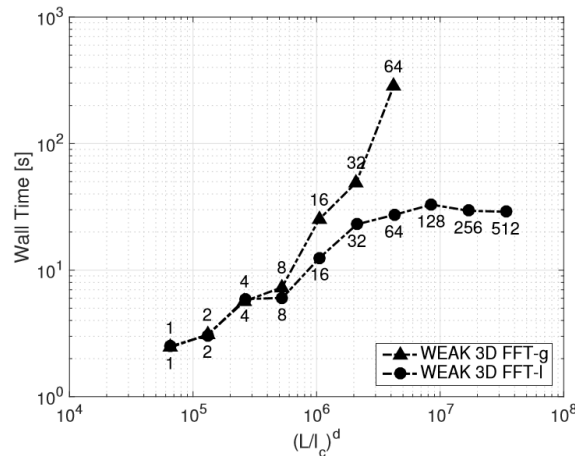
Fig 6 - Weak Scaling without localization (WEAK 3D FFT-g) and with localization (WEAK 3D FFT-l). The number on each point is the number of processors.

4.4   Parameterization in space of the random germs

One interesting advantage of the spectral representation is that it parameterizes the random field directly as a function of the strength of the heterogeneities for different wave numbers. This is interesting for identification in regimes (such as radiative transfer or diffusion) where interaction of waves and heterogeneities are determinant. However, the parameterization with phases $\hat{\phi}_n$ is not so classical. In the context of identification of mechanical properties, it is more interesting to update values of the parameters in a given area of the domain.

The impact of this parameterization is illustrated on Fig 7. Two realizations of the same random field (same statistics) are generated with exactly the same values of ϕ_n (before the Fourier transform), except in the area limited by the black circle. The two realizations are represented in the left and center plots of Fig 7. The difference between the two images (in absolute value) is plotted in the rightmost plot, with white indicating no difference. It appears clearly that the modification of the value of ϕ_n in a specific area of the grid impacts the value of the realization of the random field only in that area, as desired.
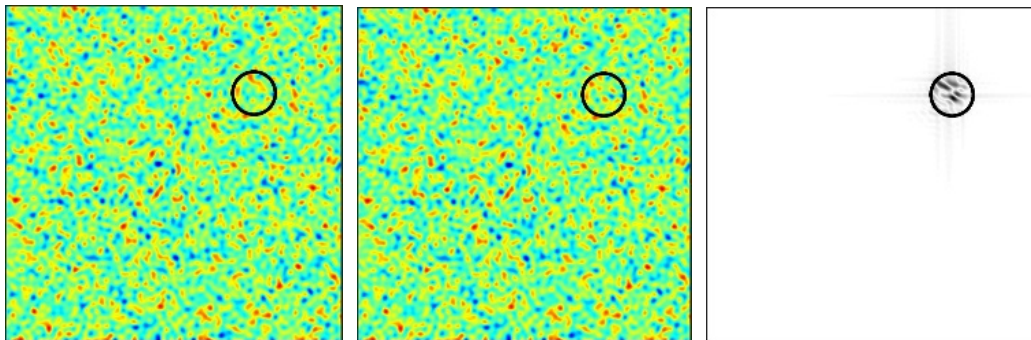

Fig 7 - The left and center plots show two realizations of a random field that only differ within the black circle. The rightmost plot shows the absolute value of the difference between the two samples (white indicates no difference).

5. Large scale mesh and wave propagation application

In this section, we illustrate the interest of the tools developed in the previous sections through wave simulations. We consider the Kefalonia region, described in Section 3.4 and aim at simulating the propagation of waves in different frequency regimes and at different levels of description of the crust.

The first model we consider is a coarse model, for a simulation in the low-frequency regime. We assume isotropic behavior and constant material parameters in the soil ($v_p = 5.8\,km/s$, $v_s = 3.2\,km/s$, $\rho =$

$2600\,kg/m^3$) and the water ($v_p = 1.4\,km/s$, $\rho = 1020\,kg/m^3$). The seismic signal is a Ricker (second derivative of a Gaussian function), centered at 0.3 Hz, and with maximum frequency close to 1 Hz. As the properties are constant with depth, no grading is necessary, except that there are two different materials. As we use 5 GLL nodes per direction and element, the element size should be approximately equal to one minimum wavelength. So we choose the element size at the bottom as $\lambda_{soil} = 6km$, and the smallest elements as $\lambda_{soil} = 2km$. This is obtained through 4 levels of refinements, and one transition layer just below the water level. The Ricker signal is translated in time by $t_0 = 3s$. Simulation results can be seen on Fig 8.
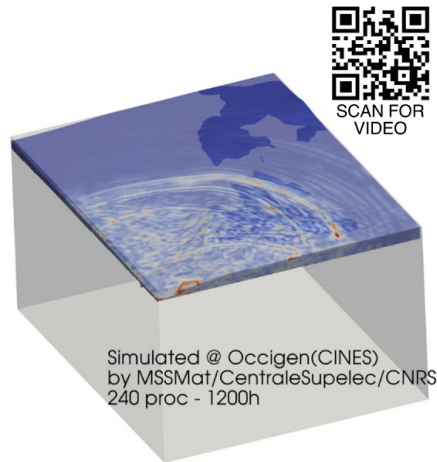

Fig 8 – Wave propagation simulation over Kefalonia (Grece) region.

6. Conclusions

In this paper we developped tools for wave propagation simulation over large heterogeneous domains. A mesher using an octree approach was tailored to take into account both bathymetry and topography. Scalability tests show that the developed mesher is suitable to simulation over large memory-distributed clusters. To represent Earth crust media heterogeneity a random field generator was built. A scalability issue in generating random properties was identified, as in the best case random field generation scales as $O(Nlog(N))$. To make random properties generation scalable the "localization method" was implemented. It glues several independently generated fields together and has a $O(N)$ scalability by block. An adaptation of the classical spectral representation allows to modify locally (in space) the value of a given realization. We consider that the developed tools, octree meshing scheme, random field generator and spectral element solver, are adapted for large scale simulations.

7. Acknowledgments

8. References

[1]   S. Schilt, J. Oliver, L. Brown, S. Kaufman, D. Albauch, J. Brewer, F. Cook, L. Jensen, P. Krumhansl, G. Long, and

D. Steiner, "The heterogeneity of the continental crust: results from deep crustal reflection profiling using the {Vibroseis} technique," *Rev. Geophys.*, vol. 17, no. 2, pp. 354–368, 1979.

[2] R.-S. Wu, Z. Xu, and X. P. Li, "Heterogeneity spectrum and scale-anisotropy in the upper crust revealed by the {German Continental Deep-Drilling (KTB)} holes," *Geophys. Res. Lett.*, vol. 21, pp. 911–914, 1994.

[3] K. Holliger, "Upper-crustal seismic velocity heterogeneity as derived from a variety of {P-wave} sonic logs," *Geophys. J. Int.*, vol. 125, no. 3, pp. 813–829, 1996.

[4] K. Shiomi, H. Sato, and M. Ohtake, "Broad-band power-law spectra of well-log data in {Japan}," *Geophys. J. Int.*, vol. 130, pp. 57–64, 1997.

[5] K.-K. Phoon and F. H. Kulhawy, "Characterization of geotechnical variability," *Can. Geotech. J.*, vol. 36, no. 4, pp. 612–624, 1999.

[6] S. Takemura, T. Furumura, and T. Maeda, "Scattering of high-frequency seismic waves caused by irregular surface topography and small-scale velocity inhomogeneity," *Geophys. J. Int.*, vol. 201, pp. 459–474, 2015.

[7] M. Meschede and B. Romanowicz, "Lateral heterogeneity scales in regional and global upper mantle shear velocity models," *Geophys. J. Int.*, vol. 200, pp. 1076–1093, 2015.

[8] A. Fichtner, *Full seismic waveform modelling and inversion*. Springer, 2012.

[9] K. Aki, "Analysis of the seismic coda of local earthquakes as scattered waves," *J. Geophys. Res.*, vol. 74, no. 2, pp. 615–631, 1969.

[10] K. Aki and B. Chouet, "Origin of coda waves: source, attenuation and scattering effects," *J. Geophys. Res.*, vol. 80, no. 23, pp. 3322–3342, 1975.

[11] M. Herraiz and A. F. Espinosa, "Coda waves: a review," *Pure Appl. Geophys.*, vol. 125, no. 4, pp. 499–577, 1987.

[12] H. Sato, M. C. Fehler, and T. Maeda, *Seismic wave propagation and scattering in the heterogeneous earth*, Second. Springer, 2012.

[13] R. L. Weaver, "Diffusivity of ultrasound in polycrystals," *J. Mech. Phys. Solids*, vol. 38, no. 1, pp. 55–86, 1990.

[14] L. Ryzhik, G. Papanicolaou, and J. B. Keller, "Transport equations for elastic and other waves in random media," *Wave Motion*, vol. 24, pp. 327–370, 1996.

[15] I. Baydoun, E. Savin, R. Cottereau, D. Clouteau, and J. Guilleminot, "Kinetic modeling of multiple scattering of elastic waves in heterogeneous anisotropic media," *Wave Motion*, vol. 51, no. 8, pp. 1325–1348, 2014.

[16] H. Bao, J. Bielak, O. Ghattas, L. F. Kallivokas, D. R. O'Hallaron, J. R. Shewchuk, and J. Xu, "Large-scale simulation of elastic wave propagation in heterogeneous media on parallel computers," *Comp. Meth. Appl. Mech. Engr.*, vol. 152, no. 1–2, pp. 85–102, 1998.

[17] D. Komatitsch, J. Ritsema, and J. Tromp, "The spectral-element method, {Beowulf} computing, and global seismology.," *Science (80-.).*, vol. 298, no. 5599, pp. 1737–1742, 2002.

[18] T. Ichimura, K. Fujita, P. E. B. Quinay, L. Maddegedara, M. Hori, S. Tanaka, Y. Shizawa, H. Kobayashi, and K. Minami, "Implicit nonlinear wave simulation with {1.08T DOF} and {0.270T} unstructured finite elements to enhance comprehensive earthquake simulation," in *Proceedings of the International Conference for High Performance Computing, Networking, Storage and Analysis (SuperComputing)*, 2015.

[19] E. Casarotti, M. Stupazzini, S. J. Lee, D. Komatitsch, A. Piersanti, and J. Tromp, "{CUBIT} and seismic wave propagation based upon the spectral-element method: an advanced unstructured mesher for complex {3D} geological media," in *Proceedings of the 16th International Meshing Roundtable*, 2008, no. 5B, pp. 579–597.

[20] T. Tu, D. R. O'Hallaron, and O. Ghattas, "Scalable parallel octree meshing for terascale applications," in *Proceedings of the 2005 ACM/IEEE Conference on Supercomputing*, 2005, pp. 1–4.

[21] H. Sundar, R. S. Sampath, S. S. Adavani, C. Davatzikos, and G. Biros, "Low-constant parallel algorithms for finite element simulations using linear octrees," in *Proceedings of the 2007 ACM/IEEE Conference on Supercomputing*, 2007, vol. 25, pp. 1–12.

[22] C. Burstedde, L. C. Wilcox, and O. Ghattas, "{\texttt{p4est}}: Scalable Algorithms for Parallel Adaptive Mesh Refinement on Forests of Octrees," *SIAM J. Sci. Comput.*, vol. 33, no. 3, pp. 1103–1133, 2011.

[23] J. J. Camata and A. L. G. A. Coutinho, "Parallel Implementation and Performance Analysis of a Linear Octree Finite Element Mesh Generation Scheme," *Concurr. Comput. Pract. Exp.*, vol. 25, pp. 826–842, 2013.

[24] I. T. Ghisi, J. J. Camata, and A. L. G. A. Coutinho, "Impact of tetrahedralization on parallel conforming octree mesh generation," *Int. J. Numer. Meth. Fluids*, vol. 75, pp. 800–814, 2014.

[25] T. Isaac, C. Burstedde, L. C. Wilcox, and O. Ghattas, "Recursive algorithms for distributed forests of octrees," *SIAM J. Sci. Comp.*, 2015.

[26] A. Pitarka and G. Ichinose, "Simulating forward and backward scattering in viscoelastic {3D} media with random velocity variations and basin structure," 2009.

[27] G. S. O'Brien and C. J. Bean, "Volcano topography, structure and intrinsic attenuation: their relative influences on a simulated {3D} visco-elastic wavefield," *J. Volcan. Geotherm. Res.*, vol. 183, no. 1–2, pp. 122–136, 2009.

[28] S. Hartzell, S. Harmsen, and A. Frankel, "Effects of {3D} random correlated velocity perturbations on predicted

ground motions," *Bull. Seism. Soc. Amer.*, vol. 100, no. 4, pp. 1415–1426, 2010.

[29]   Q.-A. Ta, D. Clouteau, and R. Cottereau, "Modeling of random anisotropic elastic media and impact on wave propagation," *Eur. J. Comp. Mech.*, vol. 19, no. 1–3, pp. 241–253, 2010.

[30]   H. Kumagai, T. Saito, G. S. O'Brien, and T. Yamashina, "Characterization of scattered seismic wavefields simulated in heterogeneous media with topography," *J. Geophys. Res. Solid Earth*, vol. 116, no. B03308, pp. 1–13, 2011.

[31]   S. Takemura and T. Furumura, "Scattering of high-frequency P wavefield derived by dense Hi-net array observations in Japan and computer simulations of seismic wave propagations," *Geophys. J. Int.*, vol. 193, no. 1, pp. 421–436, 2013.

[32]   W. Imperatori and P. M. Mai, "Broad-band near-field ground motion simulations in 3-dimensional scattering media," *Geophys. J. Int.*, vol. 192, no. 2, pp. 725–744, 2013.

[33]   E. Chow and Y. Saad, "Preconditioned {Krylov} subspace methods for sampling multivariate {Gaussian} distributions," *SIAM J. Sci. Comp.*, vol. 36, no. 2, pp. A588–A608, 2014.

[34]   V. Bouvier, L. C. Paludo, R. Cottereau, and D. Clouteau, "Scalable parallel scheme for sampling of {Gaussian} random fields over large domains," *Int. J. Numer. Meth. Engr.*, 2015.

[35]   G. Cohen, *Higher-order numerical methods for transient wave equations*. Springer, 2001.

[36]   C. Canuto, M. Y. Hussaini, A. Quarteroni, and T. A. Zang, *Spectral methods. Fundamentals in single domains*. Springer-Verlag, 2006.

[37]   K. C. Meza Fajardo, "Numerical simulation of wave propagation in unbounded elastic domains using the spectral element method," Universit{à} degli Studi di Pavia, Italy, 2007.

[38]   P. Cupillard, E. Delavaud, G. Burgos, G. Festa, J.-P. Vilotte, Y. Capdeville, and J.-P. Montagner, "{RegSEM}: a versatile code based on the spectral element method to compute seismic wave propagation at the regional scale," *Geophys. J. Int.*, vol. 188, no. 3, pp. 1203–1220, 2012.

[39]   J.-P. Berenger, "A perfectly matched layer for the absorption of electromagnetic waves," *J. Comp. Phys.*, vol. 114, no. 2, pp. 185–200, 1994.

[40]   G. Festa and J.-P. Vilotte, "The {Newmark} scheme as velocity-stress time-staggering: an efficient {PML} implementation for spectral element simulations of elastodynamics," *Geophys. J. Int.*, vol. 161, pp. 789–812, 2005.

[41]   H. Samet, *Applications of spatial data structures: computer graphics, image processing and {GIS}*. Addison-Wesley Publications, 1989.

[42]   R. Schneiders, R. Schindler, and F. Weiler, "Octree-based Generation of Hexahedral Element Meshes," in *Proceedings of 5th International Meshing Roundtable*, 1996, pp. 205–216.

[43]   R. Schneiders and R. Bünten, "Automatic generation of hexahedral finite element meshes," *Comput. Aided Geom. Des.*, vol. 12, no. 7, pp. 693–707, 1995.

[44]   T. G. Farr, P. A. Rosen, E. Caro, R. Crippen, R. Duren, S. Hensley, M. Kobrick, M. Paller, E. Rodriguez, L. Roth, D. Seal, S. Shaffer, J. Shimada, J. Umland, M. Werner, M. Oskin, D. Burbank, and D. Alsdorf, "The shuttle radar topography mission," *Rev. Geophys.*, vol. 45, no. 2, p. 2005RG000183, 2007.

[45]   "Shuttle Radar Topography Mission." .

[46]   Y. Zhang, T. J. R. Hughes, and C. L. Bajaj, "An automated {3D} mesh generation method for domains with multiple materials," *Comp. Meth. Appl. Mech. Engr.*, vol. 199, no. 5–8, pp. 405–415, 2010.

[47]   J. J. Becker, D. T. Sandwell, W. H. F. Smith, J. Braud, B. Binder, J. Depner, D. Fabre, J. Factor, S. Ingalls, S.-H. Kim, R. Ladner, K. Marks, S. Nelson, A. Pharaoh, R. Trimmer, J. von Rosenberg, G. Wallace, and P. Weatherall, "Global Bathymetry and Elevation Data at 30 Arc Seconds Resolution: {SRTM30 PLUS}," *Mar. Geod.*, vol. 32, no. 4, pp. 355–371, 2009.

[48]   "Shuttle Radar Topography Mission." .

[49]   "SRTM Water Body Database." .

[50]   Y. Zhang, C. Bajaj, and B.-S. Sohn, "{3D} finite element meshing from imaging data," *Comp. Meth. Appl. Mech. Engr.*, vol. 194, no. 48–49, pp. 5083–5106, 2005.

[51]   M. Brewer, L. Diachin, P. Knupp, T. Leurent, and D. Melander, "The mesquite mesh quality improvement toolkit," in *Proceedings of the 12th International Meshing Roundtable*, 2003, pp. 239–250.

[52]   S. Shende and A. D. Malony, "The {TAU} parallel performance system," *Int. J. High Perf. Comp. Appl.*, vol. 20, no. 2, pp. 287–311, 2006.

[53]   "TAU - Tuning and Analysis Utilities." .

[54]   M. Rosenblatt, "Remarks on a multivariate transformation," *Appl. Mech. Rev.*, vol. 23, no. 3, pp. 470–472, 1952.

[55]   M. Shinozuka and G. Deodatis, "Simulation of stochastic processes by spectral representation," *Appl. Mech. Rev.*, vol. 44, no. 4, pp. 191–205, 1991.